

Published in final edited form as:

Nat Mater. 2015 August ; 14(8): 780–784. doi:10.1038/nmat4320.

Three-dimensional imaging of dislocation propagation during crystal growth and dissolution

Jesse N. Clark^{#1,†}, Johannes Ihli^{#2}, Anna S. Schenk², Yi-Yeoun Kim², Alexander N. Kulak², James M. Campbell³, Gareth Nisbet⁴, Fiona C. Meldrum², and Ian K. Robinson^{1,5}

¹London Centre for Nanotechnology, University College, London WC1E 6BT, UK

²School of Chemistry, University of Leeds, Leeds LS2 9JT, UK.

³School of Physics and Astronomy, University of Leeds, Leeds, LS2 9JT, UK

⁴Diamond Light Source, Harwell Science and Innovation Campus, Didcot, Oxon OX11 0DE, UK

⁵Research Complex at Harwell, Didcot, Oxfordshire OX11 0DE, UK

These authors contributed equally to this work.

Abstract

Atomic level defects such as dislocations play key roles in determining the macroscopic properties of crystalline materials^{1,2}. Their effects range from increased chemical reactivity^{3,4} to enhanced mechanical properties^{5,6}. Dislocations have been widely studied using traditional techniques such as X-ray diffraction and optical imaging. Recent advances have enabled atomic force microscopy to study single dislocations⁷ in two-dimensions (2D), while transmission electron microscopy (TEM) can now visualise strain fields in three-dimensions (3D) with near atomic resolution^{8–10}. However, these techniques cannot offer 3D imaging of the formation or movement of dislocations during dynamic processes. Here, we describe how Bragg Coherent Diffraction Imaging (BCDI)^{11,12} can be used to visualize in 3D, the entire network of dislocations present within an individual calcite crystal during repeated growth and dissolution cycles. These investigations demonstrate the potential of BCDI for studying the mechanisms underlying the response of crystalline materials to external stimuli.

Keywords

Calcite; Calcium Carbonate; Imaging; Coherent Diffraction; Screw Dislocation

Users may view, print, copy, and download text and data-mine the content in such documents, for the purposes of academic research, subject always to the full Conditions of use:http://www.nature.com/authors/editorial_policies/license.html#terms

Correspondence and requests for materials should be addressed to jesclark@stanford.edu or F.Meldrum@leeds.ac.uk.

[†]Present address: Stanford PULSE Institute, SLAC National Accelerator Laboratory, 2575 Sand Hill Road, Menlo Park, California 94025, USA and Center for Free-Electron Laser Science (CFEL), Deutsches Elektronensynchrotron (DESY), Notkestrasse 85, 22607 Hamburg, Germany.

Author Contributions J.N.C. and J.I. designed the project; J.I. prepared samples; J.N.C., J.I., J.M.C., A.S.S., Y.Y.K., J.M.C., G.N. and I.K.R. performed the experiments; J.N.C. performed image reconstructions; J.N.C. & I.K.R. analyzed the Data, J.N.C., J.I., F.C.M. and I.K.R. wrote the paper. All the authors read and commented on the manuscript.

Financial Interest The authors declare no competing financial interest

Crystal growth and dissolution processes have been studied for over a century¹³, due to their significance to fields such as geology, corrosion, catalysis and the synthesis of nano-structures, through a desire to understand the link between microscopic and macroscopic processes, and due to our innate fascination with such structures. These investigations confirmed that dissolution and growth proceed by analogous mechanisms¹⁴ and also identified that crystallographic defects, and in particular screw dislocations, are of fundamental importance to crystal growth and dissolution processes¹⁵. This can be attributed to the fact that screw dislocations cause deformation (and therefore strain) of the adjacent crystal lattice, which in turn alters the activation barrier for growth and dissolution in the vicinity of the dislocation¹⁶. A full picture of crystal growth and dissolution mechanisms can therefore only be obtained by studying the relationship between the evolution of the network of dislocations within a crystal and its morphology during these processes.

In this article, we demonstrate how BCDI^{17,18} can be used to study the role of dislocations in dictating the mechanism of growth and dissolution of calcite crystals. Calcite was selected for study as it is one of the most-studied inorganic crystals, and the crystals readily grow to a few microns in size, with well-defined morphologies. BCDI is an imaging technique that uses coherent X-rays to image the density (and morphology) of a crystal, and importantly, the strain within it^{11,12}. Illumination of a crystal that is smaller than the coherence volume of the beam generates a coherent X-ray diffraction (CXD) pattern due to scattering from all parts of the crystal. An image of the crystal morphology can then be generated from the CXD pattern, where the phase of the scattered wave is reconstructed using iterative phase retrieval algorithms^{11,12,17–19}. The reconstructed density is complex valued, with the amplitude containing information about the electron density, $\rho(\mathbf{r})$. Phase shifts in the reconstructed complex density arise from strain (internal deformation) in the crystal lattice. The phase is proportional to the vector displacement field, $\mathbf{u}(\mathbf{r})$ of the atoms from the ideal lattice points and the scattering vector \mathbf{Q} via $\phi(\mathbf{r}) = \mathbf{Q} \cdot \mathbf{u}(\mathbf{r})$ (see Supplementary Information). For a single Bragg peak, a single projection of \mathbf{u} is obtained and components of \mathbf{u} perpendicular to \mathbf{Q} will not be observed. It is this sensitivity to deformations that makes BCDI ideal for studying defects within crystals.

Calcite crystals were precipitated by placing 100 μL droplets of a solution containing CaCl_2 , urea and urease on hydroxyl terminated, self-assembled monolayers (SAMs) supported on gold thin films (see Methods). CaCO_3 precipitation then occurred on enzymatic hydrolysis of the urea to ammonium and carbonate²⁰. This method was selected as it generated a high density of $\{104\}$ oriented calcite rhombohedra with average diameters of $\approx 1.25 \mu\text{m}$ ²¹. BCDI experiments were carried out at beamline I16 at the Diamond Light Source. Individual calcite crystals below 2 μm in size were illuminated with monochromatic, 8 keV X-rays, and diffraction was recorded at the $\{104\}$ Bragg peak (see Methods). 3D diffraction data sets (Supplementary Fig. 1) were obtained by rocking an isolated calcite crystal through its Bragg peak, and the same crystal was monitored while undergoing cycles of growth and dissolution. Dissolution was achieved by depositing dilute acetic acid solution on the crystal, while growth was achieved by adding a drop of calcium bicarbonate solution (see Methods). Alignment of the crystal was maintained throughout, as the X-rays were nominally

unfocussed and defined by slits with a square opening of 200 μm placed 0.3 m before the sample. This large beam size relative to crystal size also ensured that the sample was coherently illuminated²².

Figure 1 shows 3D images of the crystals as iso-surface renderings of the reconstructed amplitudes (electron density, see Supplementary Information) (a-d) and phase (projected lattice displacement) (e-h) of the initial crystal (a & e, stage i), after growth (b & f, stage ii) and after two consecutive dissolution steps (c & g, stage iii, and d & h, stage iv). The initial crystal (a) is the expected rhombohedron, which is consistent with scanning electron micrographs (Supplementary Fig. 3). Growth of this crystal (b - c) leads to an increase in size and a smoothing of the faces exposed to the bulk solution, while the face in contact with the SAM remains unchanged. Interestingly, two of the faces directed into the solution (indicated with blue arrows) grow more rapidly than the other three. This is immediately indicative of a non-uniform distribution of defects, as all faces of an entirely perfect rhombohedron would be expected to grow at the same rate. Images of the corresponding projected displacements are shown in Fig. 1 e-h, where this is mapped onto an iso-surface with red and blue representing lattice contraction or expansion respectively by half a lattice spacing. Comparison of the projected displacements before (e) and after (f) crystal growth shows that these do not grow significantly with the crystal but remain maximal at the edges. This is indicative of the presence of active growth fronts²³.

The dissolution steps (Fig. 1, b-c and c-d) show that the crystal faces retreat along all directions, but is more pronounced at certain sites (indicated by red arrows). Initial signs of changes in the crystal shape and the onset of etch-pit formation are visible after the first stage of dissolution (c), leading to an increase in the specific surface area and roughness of the crystal. The etch pits are also associated with higher levels of deformation/strain (Fig. 1 g). That relatively little change occurs in the crystal face adjacent to the substrate is consistent with the intimate contact of the SAM with this nucleation face. The second dissolution step (Fig. 1 c-d) results in a significant change in the crystal morphology, and the production of a porous isometric form²⁴ that is quite distinct from the original shape and which can be attributed to the removal of defect outcrops at the crystal surface and the coinciding etch pits formed^{25,26}. Looking at the lattice deformation, it is evident that strain present at the crystal surface reduces with the increased dissolution. This indicates that the least stable (more strained) regions dissolve first, leaving behind a more stable core (Supplementary Movies 1-4).

The projected displacement images also reveal a further feature, which is indicated by the grey arrows in Fig. 1 e-g, and is present throughout the growth and dissolution of the crystal. This region possesses both a hollow core and a spiral phase, where this combination of features is characteristic of dislocations and agrees with 2D images of dislocations obtained with TEM⁸ and Bragg ptychography²⁷. A number of these dislocations are highlighted in Fig. 2. Dislocations are characterised by a Burgers vector that measures the topological shift of the crystal along the dislocation line, where this is usually a lattice vector of the crystal²⁸. Whenever there is a component of the Burgers vector parallel to the dislocation line, it has a screw dislocation character causing the lattice to spiral around the dislocation; in this way crystal growth (and dissolution) can be facilitated. Confirmation that this feature indeed

corresponds to a screw dislocation was obtained by recording the polar angle dependence of the displacement associated with the core (indicated by the circles in Fig. 2) over the growth/ dissolution cycle of the crystal (Fig. 3 a). Although calcite is elastically anisotropic, an approximately linear relationship was observed and is consistent with what is predicted by linear elasticity theory²⁸ (see Supplementary Information). To further confirm the nature of the identified dislocation, a comparison is provided between a simulated screw dislocation and simulated screw after BCDI processing. The model screw dislocation used in the simulation is shown at atomic resolution in Fig. 4 a, with the resulting displacement of atoms from their ideal lattice positions given in Fig. 4 c. The BCDI experiment processed simulated screw dislocation is shown in Fig. 4 b and d (see Supplementary Information). Figures 4 e and f provide a comparison of BCDI reconstructed displacement and simulated displacement, viewed along the dislocation line, and clearly show that the low density core and spiral displacement are well-preserved after BCDI processing.

Further examination of regions that showed a spiral deformation and low-amplitude core enabled many additional dislocations to be identified within the imaged crystal (see Supplementary Information). These have been rendered and are shown in Fig. 5 and Supplementary Movies 5-8. In many cases the exact type of dislocation cannot be identified from a single Bragg reflection, since edge, screw and mixed dislocations will all possess qualitatively similar deformation fields. The initial crystal (Fig.5 a) possesses several dislocations which are located relatively close to the crystal surface (down to 200 nm) and are found predominantly parallel to $\{104\}$ planes. These dislocations are mainly associated with the faces exposed to the bulk solution, and are visible throughout a single crystal growth and dissolution cycle (Fig.5 , a-c), during which they (Fig.5 b) increase and (Fig.5 c) decrease in length. The reproducibility of locating the same dislocation across independently reconstructed data sets provides further credence to the recovered images.

Dislocations are often found to occur in loops or pairs with opposite Burgers vector, as this reduces the lattice potential energy and resulting long-range strain associated with these features. They also are stabilised near crystal surfaces, as found in this work, such that dislocation motion can transport material into and out of crystals from the growth solution²⁹. As intuitively expected, the most rapidly growing crystal faces were observed to have the highest number of surface dislocations. The distribution of these defects within the crystal therefore plays a part in determining the morphology of the product crystal. Considering the dissolution process, the locations of the dislocations coincide with the position of the etch pits that appear at the crystal surface during dissolution. This suggests that the developing pits follow the cores of the dislocations, where this effect can be attributed to a reduced activation barrier to dissolution due to stored strain energy in the defects¹⁴. New dislocations could be identified during the dissolution (Fig. 5 c-d), and by the final stage (Fig. 5 d) many of the original dislocations had been annihilated. The loss of faceting and dislocations near the surface support the hypothesis that the least stable regions dissolve first, leaving behind a more stable core.

To determine the overall effect that the growth/ dissolution had on the strain and deformation of the crystal, the gradient of the displacement was calculated and its magnitude was plotted as a function of fractional size (Fig, 3 b and c). The magnitude of the gradient

was calculated over successively larger shells and averaged over all directions and is plotted as a % of deformation (strain) relative to the lattice constant for the 104 reflection (see Supplementary Information) for the directions parallel and perpendicular to the scattering vector. What is evident (Fig. 3 b and c) is that the initial crystallite experiences an increasing strain from the center, outwards. This can be compared to a crystal formed after the first growth stage (Fig. 1 f), which shows an overall flatter initial strain, and then increases more rapidly above a fractional size ≈ 0.6 . The smoother transition and lower strain for the direction parallel suggest some relaxation of the crystal after the initial growth and can also be seen in the slices in Fig. 2. The non-zero strain perpendicular to the scattering vector is indicative of a shear strain, although we only have a single Bragg peak so the full strain tensor cannot be obtained and the exact nature of this cannot be determined. These data are consistent with the assertion that the effect of the surface only penetrates to a finite distance into a crystal. With the increased roughness and etch-pit formation that occurs in the first dissolution step (Fig. 1 g), the overall strain is higher, demonstrating that these surface features affect the entire crystal, leading to an increase in overall deformation. After the final dissolution (Fig. 1 h) when the majority of surface dislocations have been removed, the strain becomes almost flat. This indicates that surface effects are less pronounced, despite the increased relative surface area.

With its ability to simultaneously generate 3D images of the strain within a crystal and the gross crystal morphology, BCDI provides an extremely powerful way of visualising the network of dislocations present within an individual crystal. Importantly, BCDI can be performed in the absence of any sample preparation, which means that it can be used to elucidate the effects of dislocation networks on dynamic crystal behaviour. Using the example of crystal growth and dissolution, we have located dislocations within calcite single crystals, and then demonstrated that their distribution within the crystal dictates rapidly-growing directions. Conversely, preferential dissolution and etch pit formation was also observed within the vicinity of the dislocations, which provides evidence that the stored energy within the dislocations affects the crystal response. The ability to view these fundamental processes using BCDI represents an important step forward in elucidating the nanoscale mechanisms underlying crystallisation processes. Importantly, BCDI also opens the door to 3D visualisation of the role of dislocations in the response of a crystal to a huge range of experimental conditions, such as temperature changes or mechanical force.

Methods

Materials and General Preparative Methods

Analytical grade, $\text{CaCl}_2 \cdot 2\text{H}_2\text{O}$, Acetic Acid, Urea and Urease (canavalia ensiformis, subunit molecular weight: ~ 90.770 kDa) were purchased from Sigma-Aldrich and were used as received. Aqueous solutions were prepared using Milli-Q Standard 18.2 M Ω cm. Solutions of 11-Mercapto-1-undecanol (Sigma-Aldrich) were freshly prepared in laboratory grade ethanol, and experiments were performed at a constant temperature of 21°C. Reagent containing glassware was soaked overnight in 10% w/v NaOH, followed by rinsing with dilute HCl and washing with Milli-Q water.

Substrate Preparation

Glass slides and crystallizing dishes were placed overnight in Piranha solution (70:30 %wt. sulfuric acid: hydrogen peroxide) and were then washed copiously with Milli-Q water before being exposed to the crystallisation solution. Functionalized self-assembled monolayers (SAMs) were prepared on freshly deposited noble metal films. Thin films were deposited either on silicon wafers using a Mantis Qprep 250 deposition system or a Cressington 308R coating system at a base pressure below 10^{-6} mbar. 2 nm of Cr were initially deposited to promote substrate adhesion, followed by the evaporation of 50 nm of Au (Goodfellow, 99.99%) at 0.1 nm/s. SAMs were then prepared by immersing a prepared metal substrate in 1 mM thiol solution in ethanol, at room temperature for 24 h in the dark. The SAMs were then thoroughly rinsed with ethanol and Milli-Q water and were dried under nitrogen before usage.

Mineral Deposition

Preferentially oriented calcite was obtained by adding 350 μL urease (1 mg mL^{-1}) to 1 mL of 5 mM CaCl_2 / 20 mM urea. Separate droplets (100 μL) of the resulting aqueous solution were subsequently placed on the prepared SAM, and stored at 100% r.h.. Hydroxyl-terminated SAMs were used as the crystallization substrate to obtain calcite rhombohedra that were principally {104} oriented. Enzymatic hydrolysis of urea to ammonium and carbonate creates the required supersaturation profile, where the gradual increase in supersaturation ensures that a sufficient density of single crystal particles of CaCO_3 is obtained.

Overgrowth of Initial Deposits

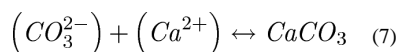
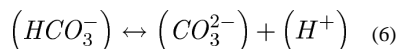
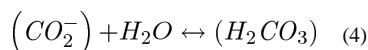
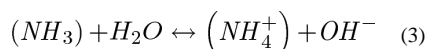
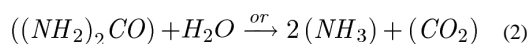
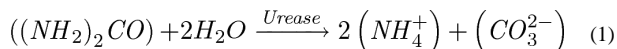
Observations of crystal growth were carried out on samples which had previously been centered into the Bragg condition. A 50 μL volume of ≈ 1 mM calcium bicarbonate solution was pipetted onto the sample, where evaporation and CO_2 out-gassing results in a supersaturation increase which causes crystal growth. After evaporation of the droplet, the selected crystals were then re-analyzed. Calcium bicarbonate solutions were prepared according to the method of Kitano³⁰. 100 mg of CaCO_3 were added to one litre of Milli-Q water. $\text{CO}_2(\text{g})$ was then bubbled through this solution for three hours followed by filtering through a 200 nm Isopore GTTP membrane filter (Millipore) resulting in an initial pH of 6.4.

Partial Dissolution

Dissolution of BCDI imaged calcite crystals was achieved by depositing 50 μL of 0.1 wt% acetic acid solution onto a 0.4 cm^2 substrate with an estimated number density of 0.1 crystals/ μm^2 with an average size of 1 μm . The solution was then removed after 60 seconds. This was followed by addition and removal of a drop of ethanol to wash the sample, and a further diffraction pattern was collected (see Supplementary Fig. 4). The process was then repeated between two and three times to obtain diffraction data for successive dissolution stages of the initially imaged single crystal.

Enzymatic Hydrolysis (Urea-Urease) catalyzed Precipitation

Calcium carbonate deposition using the enzymatic hydrolysis of urea by urease, and droplets placed on the substrate, allows controlled precipitation of crystals independent of droplet wetting behavior and gas-liquid interface area³¹. By variation of the urea and urease concentrations, which determines the rate of production of carbonate and ammonium, the rate of production of CaCO₃ can be controlled. A slow increase in supersaturation was required to give crystals that were principally unstrained and which were present in a high enough number density to enable crystals to be easily located on the substrate during BCDI imaging. The key underlying reactions are presented below.



External Characterization

CaCO₃ precipitates at different growth and dissolution stages were characterised by Scanning Electron Microscopy (SEM). Electron micrographs of uncoated specimen were obtained using a FEI Nova NanoSEM 650. Crystal growth and dissolution rates of outgrown individual calcite crystal were obtained using an inverted Olympus IX-70 confocal microscope.

Experimental Setup

BCDI experiments were performed at Beamline I-16 at the Diamond Light Source (DLS) UK. An undulator produced X-rays which were monochromatized to an energy of 8 keV using a channel-cut Si(111) monochromator. Calcite crystals supported on substrates were placed on a diffractometer which had its rotation centre aligned with the X-ray beam. Slits were used to reduce the area illuminated by the X-rays. An X-ray sensitive, CMOS pixel

detector (Medipix3) with 256×256 square pixels of side length $55 \mu\text{m}$ was positioned at the desired diffraction angle for an off-specular $\{104\}$ reflection at a distance of 2.7 m from the sample. An evacuated flight tube was placed between the detector and sample to reduce air absorption and scatter. To measure its full 3D diffraction pattern, the crystal was rotated by 0.3° with a 0.003° degree step size. A two-dimensional slice of the 3D far-field diffraction pattern was recorded at each angle of rotation using an exposure time of 1 second. By stacking all of these two-dimensional diffraction frames together, a complete 3D diffraction pattern was obtained, from which real-space images can be reconstructed (see Supplementary Information). Due to the small size of the crystals, $\sim 1\text{--}2 \mu\text{m}$, the illumination can be considered to be almost completely coherent. To ensure that the same crystal could be analysed over a growth/ dissolution cycle, a local search in reciprocal space was performed to pick an isolated single crystal. This ensured that there was little chance of a signal originating from another crystal overlapping the original crystal diffraction.

Supplementary Material

Refer to Web version on PubMed Central for supplementary material.

Acknowledgements

This work was supported by FP7 advanced grant from the European Research Council (J.N.C. and I.K.R.) and an Engineering and Physical Sciences Research Council Leadership Fellowship (F.C.M. and J.I.). It was also funded through an EPSRC Programme Grant (A.S.S. and F.C.M., EP/I001514/1) which funds the Materials in Biology (MIB) consortium, and EPSRC grants EP/J018589/1 (YYK) and EP/K006304/1 (ANK). We thank Diamond Light Source for access to Beamline I-16 (MT 8187, MT 7654 and MT 7277) that contributed to the results presented here.

References

1. Stoneham, A. Theory of Defects in Solids. Clarendon; Oxford: 1985.
2. Burton C. A theory concerning the constitution of mater. *Phil. Mag.* 1892; 33:191–203.
3. Lasaga AC, Lutge A. Variation of crystal dissolution rate based on a dissolution stepwave model. *Science.* 2001; 291:2400–2404. [PubMed: 11264534]
4. De Yoreo JJ, Vekilov PG. Principles of crystal nucleation and growth. *Reviews in Mineralogy and Geochemistry.* 2003; 54:57–93.
5. Ma E, Shen TD, Wu XL. Nanostructured metals: Less is more. *Nat Mater.* 2006; 5:515–516. [PubMed: 16819470]
6. Kunitake ME, Mangano LM, Peloquin JM, Baker SP, Estroff LA. Evaluation of strengthening mechanisms in calcite single crystals from mollusk shells. *Acta Biomaterialia.* 2013; 9:5353–5359. [PubMed: 23036948]
7. Davis KJ, Dove PM, De Yoreo JJ. The role of mg^{2+} as an impurity in calcite growth. *Science.* 2000; 290:1134–1137. [PubMed: 11073446]
8. Hytch MJ, Putaux J-L, Penisson J-M. Measurement of the displacement field of dislocations to 0.03 nm by electron microscopy. *Nature.* 2003; 423:270–273. [PubMed: 12748637]
9. Barnard JS, Sharp J, Tong JR, Midgley PA. High-resolution three-dimensional imaging of dislocations. *Science.* 2006; 313:319. [PubMed: 16857932]
10. Chen C-C, et al. Three-dimensional imaging of dislocations in a nanoparticle at atomic resolution. *Nature.* 2013; 496:74–77. [PubMed: 23535594]
11. Pfeifer MA, Williams GJ, Vartanyants IA, Harder R, Robinson IK. Three-dimensional mapping of a deformation field inside a nanocrystal. *Nature.* 2006; 442:63–66. [PubMed: 16823449]

12. Robinson I, Harder R. Coherent x-ray diffraction imaging of strain at the nanoscale. *Nat Mater.* 2009; 8:291–298. [PubMed: 19308088]
13. Weeks, JD.; Gilmer, GH. *Advances in Chemical Physics.* John Wiley and Sons, Inc.; 2007. Dynamics of crystal growth; p. 157-228.
14. Dove PM, Han N. Kinetics of mineral dissolution and growth as reciprocal microscopic surface processes across chemical driving force. *AIP Conference Proceedings.* 2007; 916:215–234.
15. Frank FC. The influence of dislocations on crystal growth. *Discussions of the Faraday Society.* 1949; 5:48–54.
16. Brantley, SL. Kinetics of mineral dissolution. In: Brantley, SL.; Kubicki, JD.; White, AF., editors. *Kinetics of Water-Rock Interaction.* Springer; New York: 2008. p. 151-210.
17. Clark JN, et al. Ultrafast three-dimensional imaging of lattice dynamics in individual gold nanocrystals. *Science.* 2013; 341:56–59. [PubMed: 23704372]
18. Cha W, et al. Core-shell strain structure of zeolite microcrystals. *Nat Mater.* 2013; 12:729–734. [PubMed: 23832126]
19. Fienup JR. Phase retrieval algorithms: a comparison. *Applied Optics.* 1982; 21:2758–2769. [PubMed: 20396114]
20. Antipov A, et al. Urease-catalyzed carbonate precipitation inside the restricted volume of polyelectrolyte capsules. *Macromolecular Rapid Communications.* 2003; 24:274–277.
21. Lee JRI, et al. Structural development of mercaptophenol self-assembled monolayers and the overlying mineral phase during templated CaCO_3 crystallization from a transient amorphous film. *J. Am. Chem. Soc.* 2007; 129:10370–10381. [PubMed: 17672454]
22. Clark JN, Huang X, Harder R, Robinson IK. High-resolution three-dimensional partially coherent diffraction imaging. *Nat Commun.* 2012; 3:993. [PubMed: 22871812]
23. Paquette J, Reeder RJ. Relationship between surface structure, growth mechanism, and trace element incorporation in calcite. *Geochimica et Cosmochimica Acta.* 1995; 59:735–749.
24. Snyder RC, Doherty MF. Faceted crystal shape evolution during dissolution or growth. *AIChE Journal.* 2007; 53:1337–1348.
25. MacInnis IN, Brantley SL. The role of dislocations and surface morphology in calcite dissolution. *Geochimica et Cosmochimica Acta.* 1992; 56:1113–1126.
26. MacInnis IN, Brantley SL. Development of etch pit size distributions on dissolving minerals. *Chemical Geology.* 1993; 105:31–49.
27. Takahashi Y, et al. Bragg x-ray ptychography of a silicon crystal: Visualization of the dislocation strain field and the production of a vortex beam. *Phys. Rev. B.* 2013; 87:121201.
28. Hirth, JP.; Lothe, J. *Theory of Dislocations.* McGraw-Hill; New York: 1968.
29. Pun GP, Mishin Y. A molecular dynamics study of self-diffusion in the cores of screw and edge dislocations in aluminum. *Acta Materialia.* 2009; 57:5531–5542.
30. Kitano Y, Park K, Hood DW. Pure aragonite synthesis. *J. Geophys. Res.* 1962; 67:4873–4874.
31. Ihli J, Bots P, Kulak A, Benning LG, Meldrum FC. Elucidating mechanisms of diffusion-based calcium carbonate synthesis leads to controlled mesocrystal formation. *Advanced Functional Materials.* 2013; 23:1965–1973.

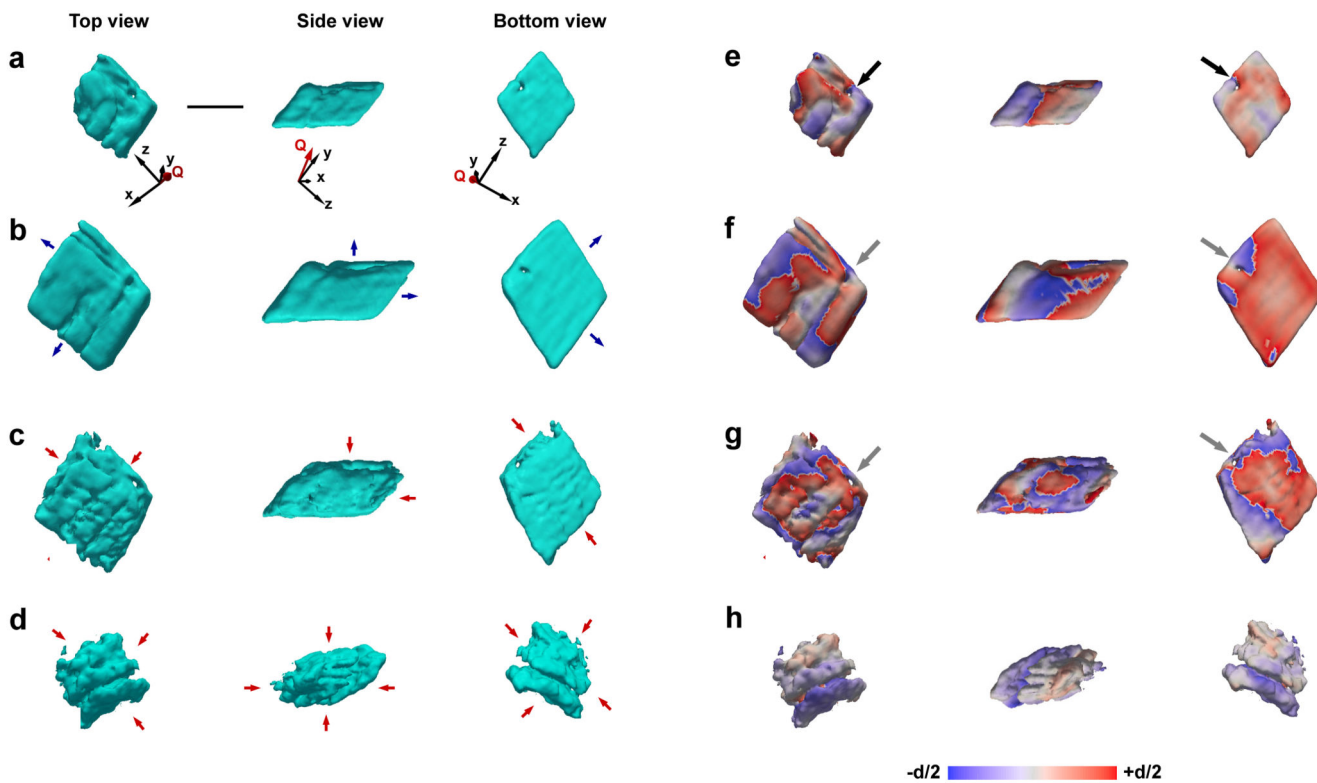


Figure 1. Growth and dissolution of calcite observed by BCDI

Shown is an iso-surface rendering of the (a-d) electron density (reconstructed amplitude) and (e-h) projected displacement (phase) from initially deposited calcite crystal (a & e, stage i), after secondary growth (b & f, stage ii), and after consecutive dissolution steps (c & g, stage iii, and d & h, stage iv). The scale bar is $1 \mu\text{m}$. Three different viewing angles of the crystal are shown - top down (left), side (middle panel) and bottom up (right). The substrate would be on the bottom of the crystal shown in the side view. Perspectives highlight the shape transition that occurs during growth (a-b & e-f) and dissolution (b-d & f-h). Prominent surface advance (growth, blue arrows) and retreat (dissolution, red arrows) directions are shown. The gray arrow points towards the primary dislocation continuously identifiable during crystal growth and dissolution (a-c & e-g). The beam direction is along the z axis, with the y axis vertical. The scattering vector (\mathbf{Q}) is shown in red.

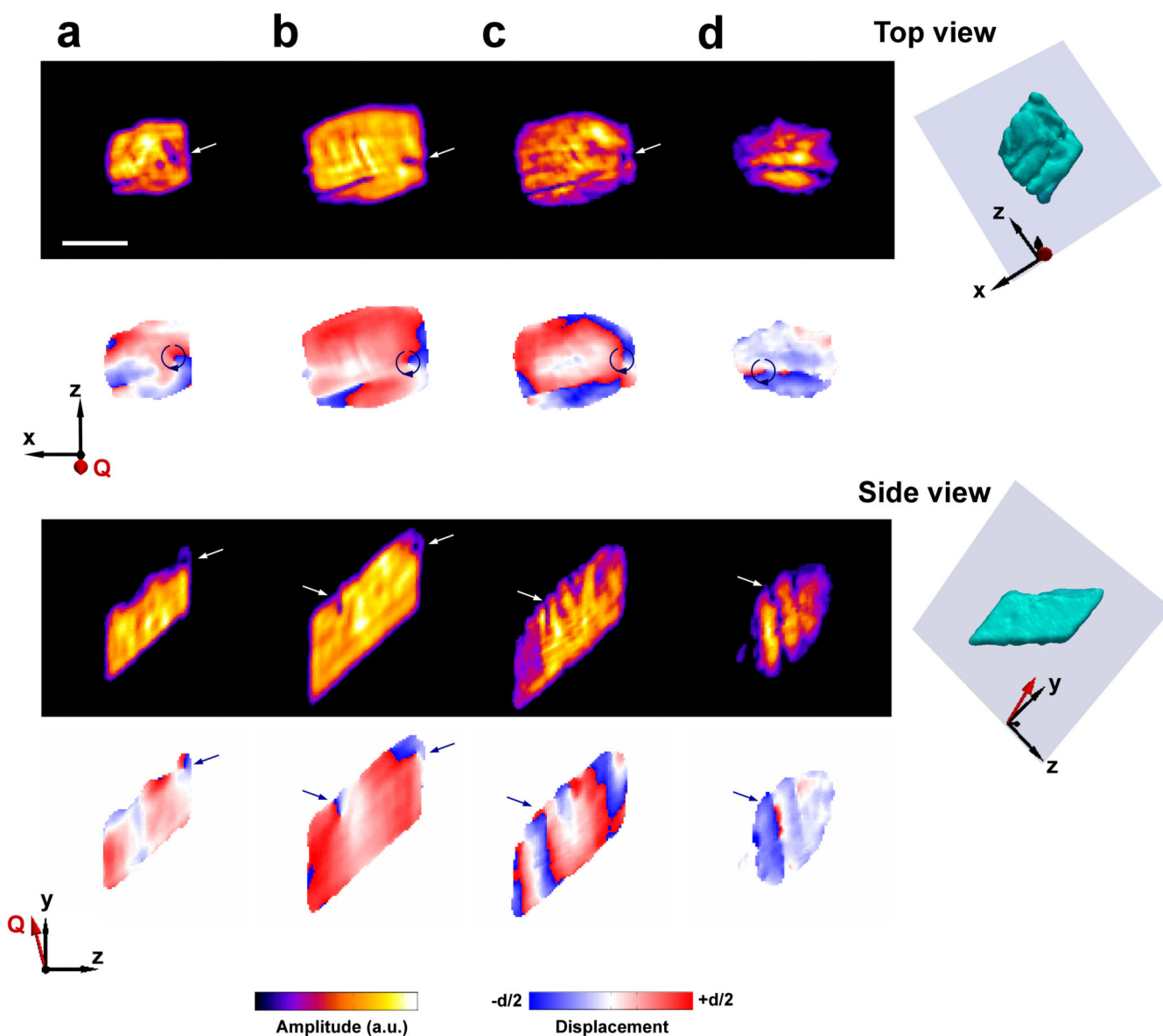


Figure 2. Slices showing the electron density and projected displacement during growth and dissolution

Shown is the initial crystal (a), after growth (b) and repetitive dissolution steps (c & d) for two viewing directions (top view) and (side view). The amplitude is shown in the top rows (black background) with the dislocations highlighted by white arrows featuring a low-amplitude core. The phase presented in the bottom rows also shows selected dislocations highlighted by the dark blue arrows. Particularly evident is the spiral phase (displacement) that is characteristic of a screw dislocation. The iso-surface to the right shows the location of the cut-planes. The scale bar is $1 \mu\text{m}$.

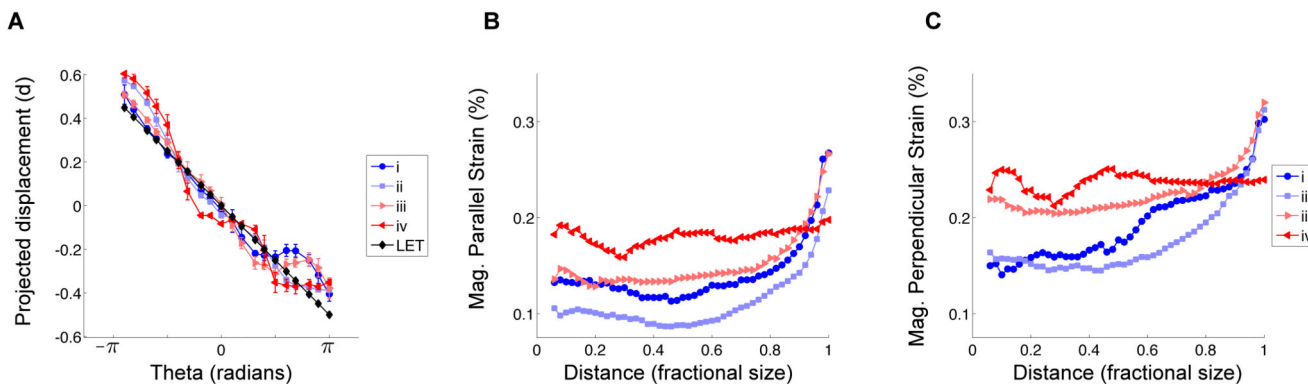


Figure 3. Displacement and strain magnitude line plots

Plotted in (a) is the recovered projected displacement measured at development stages (i-iv) as a function of theta for the dark blue circles with arrows from Fig. 2 a. This is compared to the displacement expected by linear elasticity theory (LET). The error bars represent the standard deviation ($\pm\sigma$) of the displacement over adjacent layers spanning a region of 200 nm along Q . (b) The magnitude of the strain component parallel and perpendicular (c) to the scattering vector over the growth/dissolution cycle (i-iv) plotted as a function of fractional crystal size (center of the crystal 0 to crystal surfaces 1). This graph highlights the diminishing relevance of surface effects with (ii) growth of the crystal, and its increasing relevance with (iii & iv) dissolution. The strain is calculated as the magnitude of the gradient of the displacement and averaged over successively larger shells.

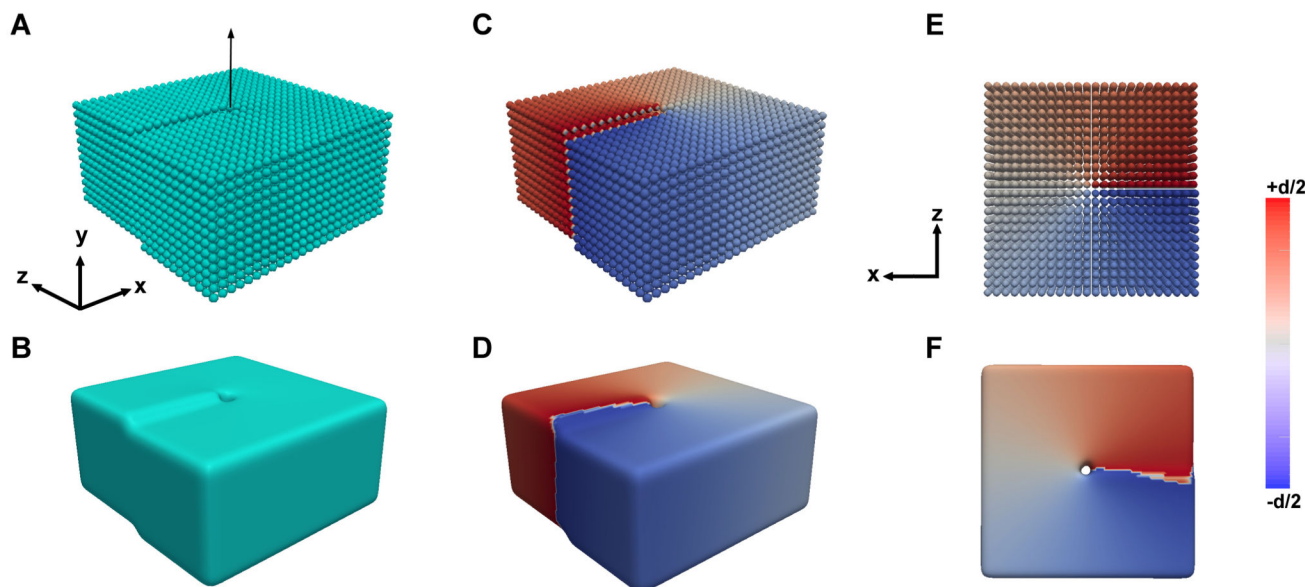


Figure 4. Simulation of a screw dislocation

Iso-surface rendering of a screw dislocation (a) with atomic resolution, and by filtering (b) the Fourier transform of (a) with a Gaussian centred on the (0,1,0) Bragg peak, replicating the BCDI experiment. The displacement is rendered onto the iso-surface for the atomic resolution (c) and the phase is rendered onto the surface for the BCDI simulation (d) showing the spiral phase centred around the dislocation core. (e) and (f) show another view of the dislocation for the atomic resolution (e) and BCDI experiment (f), revealing the low density region at the core in the BCDI experiment simulation. It should be noted that for the atomic resolution the displacement is mapped onto the iso-surface where for the BCDI example, the resultant phase is mapped on to the iso-surface.

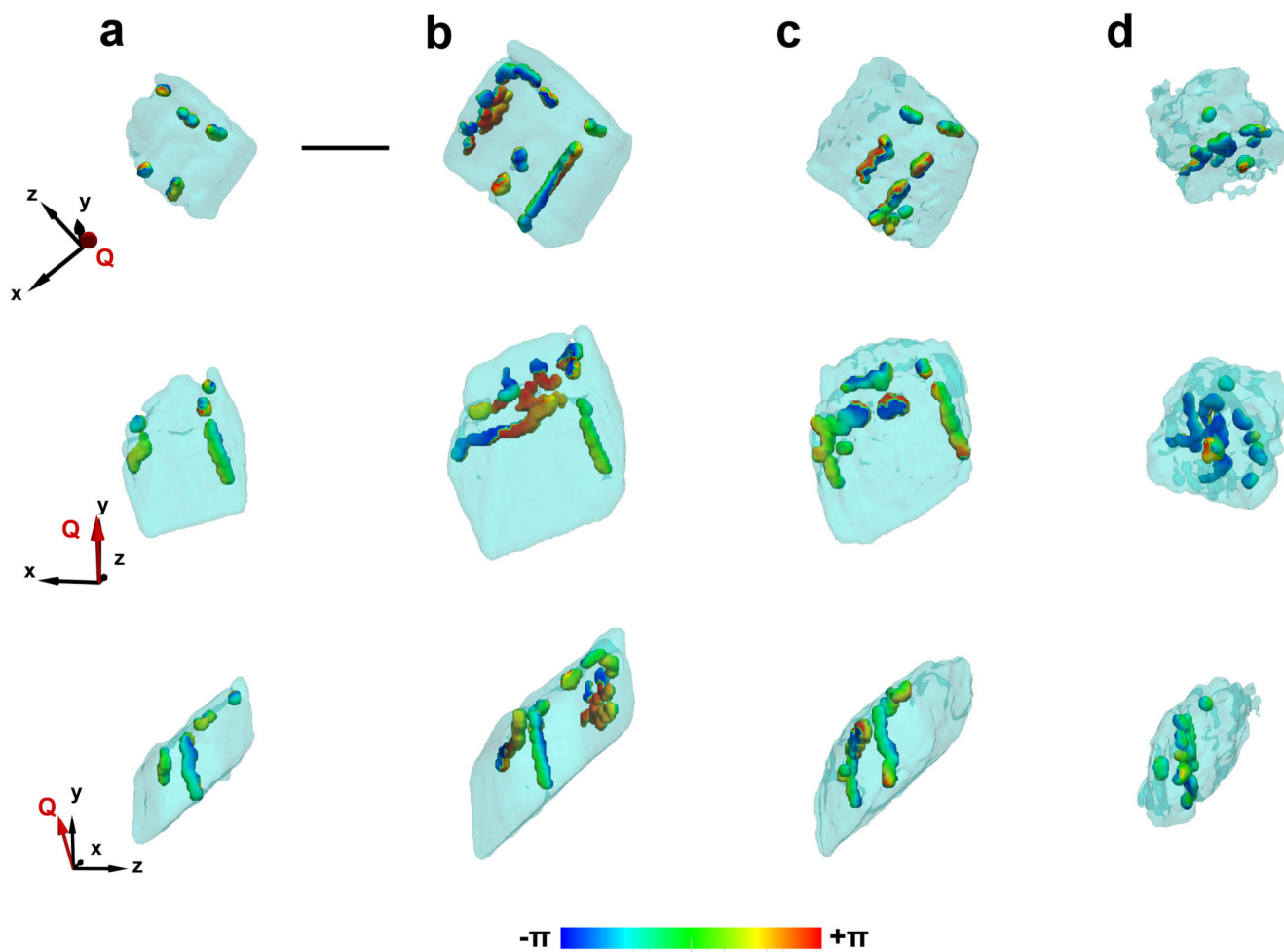


Figure 5. Iso-surface rendering of defect network within a calcite crystal

Iso-surface renderings of dislocations present within the crystal imaged (a) before and after (b) growth, and (c-d) after dissolution. The scale bar is $1 \mu\text{m}$. The evolution of the dislocations is evident through crystal growth (a-b) and dissolution (b-c & c-d), where these are shown from left to right. Three different viewing angles of the crystals are provided (vertically, top to bottom) - from the base, above and the side. Dislocations are predominantly located near the surface and on the faces that grow most rapidly. The phase has been mapped to the iso-surfaces of present dislocations, showing the characteristic spiral.